Supplementary materials

Experimental section

Chemical and Materials:

1,3-Dioxlane (DOL, battery grade, $H_2O \leq 20$ ppm), fluoroethylene carbonate (FEC, battery grade, $H_2O \leq 20$ ppm), bis(trifluoromethane)sulfonimide lithium (LiTFSI, battery grade) and lithium hexafluorophosphate ($LiPF_6$, battery grade) were obtained from DoDo Chem. Lithium difluorophosphate ($LiPO_2F_2$, ≥98%) was purchased from Aladdin. Copper foil, carbon-coated aluminum foil, lithium foil, poly(vinylidence fluoride) (PVDF), N-methyl-2-pyrrolidone (NMP), Super-P conductive carbon, and ceramic-coated polyethylene separator were used as received without further purification.

Preparation of precursor electrolyte of quasi-solid-state electrolyte without plasticizer:

The precursor electrolyte was prepared by dissolving 2 M LiTFSI in DOL solvent within an argon-filled glove box at room temperature. Subsequently, 0.1 M lithium salt initiator was introduced and fully dissolved. Polymerization was allowed to proceed by standing the mixture at room temperature until complete solidification.

Preparation of precursor electrolyte of quasi-solid-state electrolyte (F6-PDOL, F2-PDOL):

The precursor electrolyte was prepared by dissolving 2 M LiTFSI in a mixed solvent of DOL and FEC (7:3, v/v) within an argon-filled glove box at room temperature. To obtain F2-PDOL, 0.1 M $LiPO_2F_2$ was subsequently added and dissolved, and the mixture was allowed to polymerize by standing at room temperature until fully solidified. For F6-PDOL, $LiPO_2F_2$ was substituted with $LiPF_6$ at the same concentration, followed by an identical polymerization procedure.

All electrolytes were prepared and sealed in an Ar-filled glovebox ($H_2O < 0.1$ ppm, $O_2 < 0.1$ ppm) under identical conditions. While the absolute water content was not specifically measured, the consistent environment ensures that the comparative conclusions regarding polymerization behavior and ion transport properties are robust and based on the chemical additive effect rather than incidental water variation.

Materials Characterization:

The morphology of electrodeposited lithium was investigated by scanning electron microscopy (SEM). The chemical composition of the solid electrolyte interphase (SEI) and cathode electrolyte interphase (CEI) formed on cycled lithium anodes and NCM811 cathodes was characterized by X-ray photoelectron spectroscopy (XPS) using monochromated Al Kα radiation. Raman spectroscopy (Thermo Fisher, DXR3xi) was used to monitor the composition change of the electrolyte. Nuclear magnetic resonance (NMR) spectroscopy was employed to analyze the composition of the electrolyte before and after polymerization. The molecular weight of the synthesized PDOL was determined by gel permeation chromatography (GPC). Thermal properties were evaluated via simultaneous thermogravimetric analysis and differential scanning calorimetry (TGA-DSC) at a heating rate of 10 $K \cdot min^{-1}$ under a nitrogen atmosphere.

Electrochemical Measurement:

Electrochemical performance was evaluated using CR2032 coin cells assembled with 60 μL of precursor electrolyte and a ceramic-coated polyethylene separator. All tests were conducted at 30 °C unless specified otherwise.

For Coulombic efficiency (CE) measurements, Cu foil was used as the working electrode and Li foil as the reference/counter electrode. Cells were cycled at 0.5 mA cm^{-2} with a fixed areal capacity of 0.5 mAh cm^{-2} and a cut-off voltage of 0.8 V. Linear sweep voltammetry (LSV) was performed in cells with stainless steel as the working electrode and Li foil as both reference and counter electrode, scanning from 3 V to 6 V (vs. Li^+/Li) at 0.5 mV s^{-1} using a Gamry electrochemical workstation. Symmetric Li/Li cells were cycled at 0.5 mA cm^{-2} and 0.5 mAh cm^{-2} using a LAND battery test system (Wuhan, China). For full-cell tests, cathodes were prepared by blending $LiFePO_4$ (LFP) or $LiNi_{0.8}Co_{0.1}Mn_{0.1}O_2$ (NCM811) powder with Super-P conductive carbon and PVDF binder in an 8:1:1 weight ratio. Long-term cycling and rate tests were carried out within voltage windows of 2.5-4.0 V for LFP/Li cells and 2.8-4.3 V for NCM811/Li cells. Cyclic voltammetry (CV) of LFP/Li cells was recorded on a CHI760E instrument (Shanghai, China) between 2.5 and 4.0 V, with scan rates incrementally increased from

0.1 to 0.4 mV s^{-1}. Electrochemical impedance spectroscopy (EIS) was performed using a Gamry workstation with a 10 mV amplitude under open-circuit conditions; the resulting spectra were deconvoluted via distribution of relaxation times (DRT) analysis [1,2]. The temperature dependence of ionic conductivity was fitted using the Vogel-Tammann-Fulcher (VTF) equation:

$$\sigma = \sigma_0 T^{-\frac{1}{2}} \exp(-\frac{E_a}{R(T-T_0)})$$

where σ_0 is the pre-exponential factor, E_a represents the activation energy, T_0 denotes the effective glass transition temperature, and R is the ideal gas constant.

Density Functional Theory (DFT) Calculation:

All DFT calculations were carried out using the DMol^3 module within Materials Studio. The exchange-correlation energy was treated with the Becke three-parameter hybrid functional combined with the Lee-Yang-Parr correlation functional (B3LYP) [3,4]. DFT A double-numerical plus polarization (DNP) basis set with DFT semi-core pseudopotentials and a 4.4 basis file were employed. Geometry optimizations were considered converged when the forces on atoms fell below 0.002 Ha $Å^{-1}$ and the energy difference between successive steps was less than 1.0×10^{-5} Ha, with a displacement convergence criterion of 0.005 Å. The conductor-like screening solvation model (COSMO) was included in all calculations. The binding energy (ΔE) between species A and B was calculated as:

$$\Delta E = E_{total} - E_A - E_B$$

Where E_{total} is the total energy of the optimized A-B complex, and E_A and E_B are the energies of the isolated species A and B, respectively.

To reduce computational cost while retaining representative features of the polymer environment, the PDOL chain was modeled by a segment containing five repeating DOL units.

Molecular Dynamics (MD) simulation:

All MD simulations were carried out using the Forcite module with the COMPASS III force field in Materials Studio [5]. Van der Waals and Coulomb interactions were

respectively considered by atom based and Ewald methods with a cut-off value of 18.5 Å. The equations of motion were integrated with a time step of 1 fs. Following energy minimization, each system was equilibrated under periodic boundary conditions in the NPT ensemble (P = 1 atm) for 500 ps (first at 333.15 K for 200 ps, then at 303.15 K for 300 ps) using the Nosé-Hoover thermostat and Berendsen barostat. This procedure ensured the stabilization of system temperature, potential energy, and total energy. After equilibration, a production run of 1000 ps in the NVT ensemble was conducted for the analysis of radial distribution functions (RDFs) and coordination numbers (CNs). The F2-PDOL and F6-PDOL electrolyte systems, each composed of components listed in Table S1, were constructed in separate cubic simulation boxes. We note that while the actual PDOL chains have different molecular weights, the MD simulations focus on local solvation structures, which are dominated by nearest-neighbor oxygen atoms and are well-captured by a pentamer model. [6]

Table S1. Number of solution components.

Electrolyte	Li^+	$TFSI^-$	DOL	PDOL (pentamer)	FEC	$PO_2F_2^-$	PF_6^-
F2-PDOL	105	100	63	88	206	5	0
F6-PDOL	105	100	63	88	206	0	5

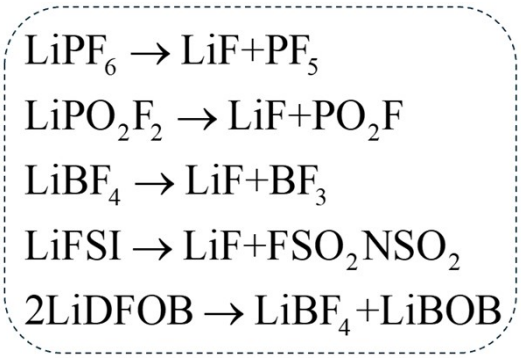

Fig. S1. Chemical process depicting the generation of Lewis acid intermediates from the decomposition of lithium salt initiators.

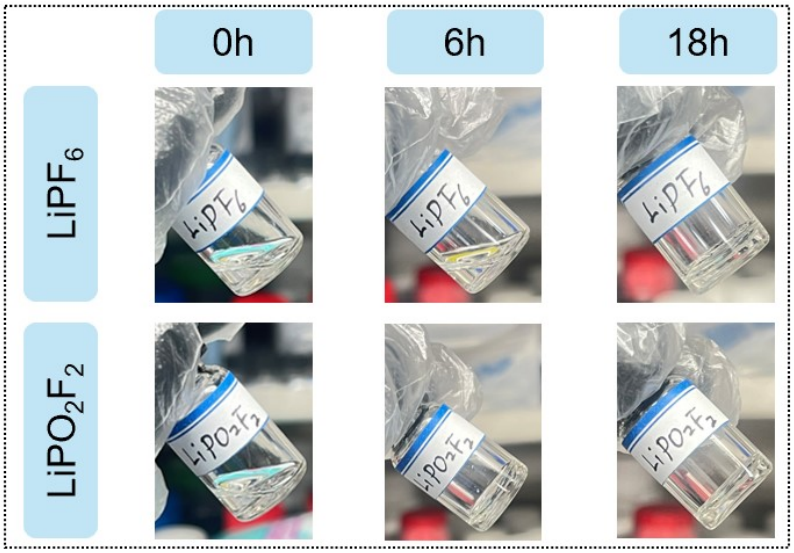

Fig. S2. Photographs show the solidification progress of precursor solutions containing $LiPF_6$ or $LiPO_2F_2$ as initiators over time.

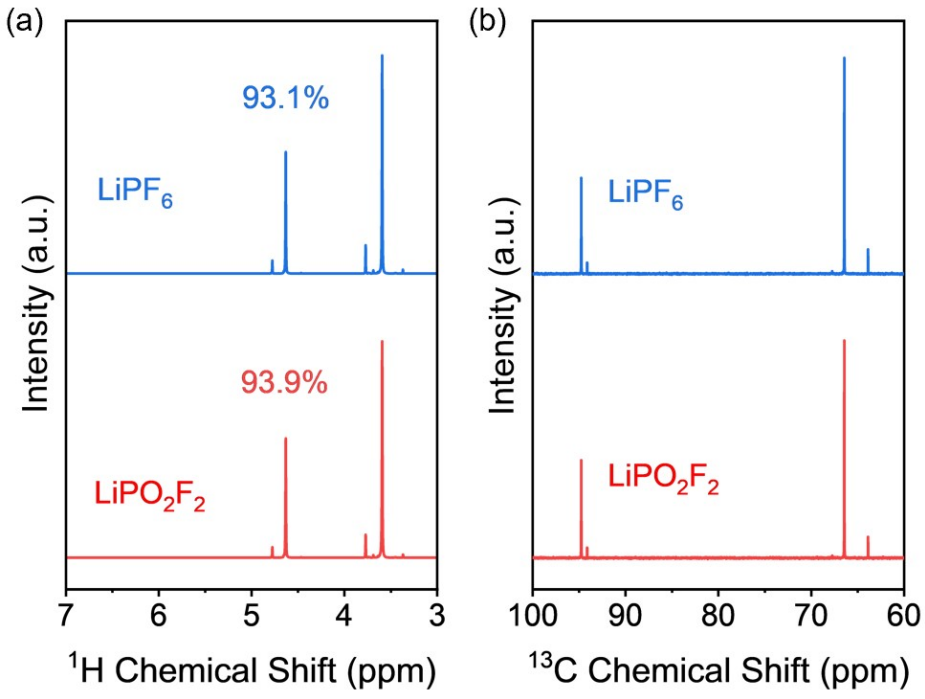

Fig. S3. (a) ^{1}H NMR and (b) ^{13}C NMR spectra of $LiPF_6$ and $LiPO_2F_2$ initiated PDOL electrolyte.

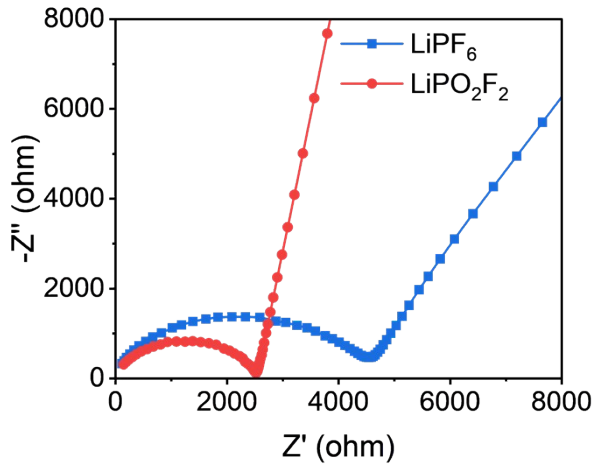

Fig. S4. Nyquist plots at 30 °C of the in-situ polymerized PDOL electrolyte.

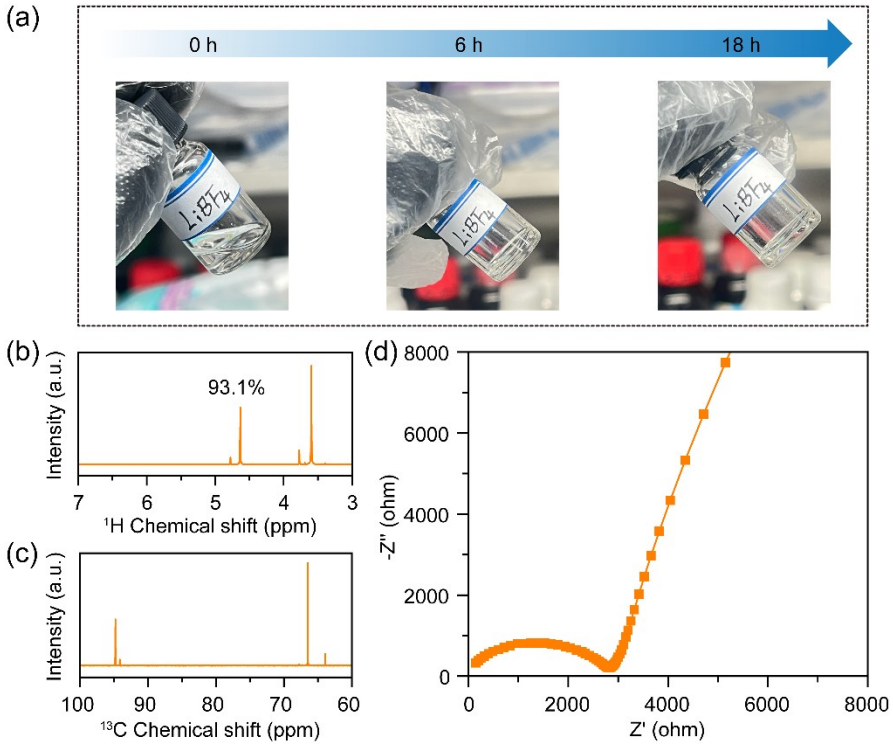

Fig. S5. Experimental and computational validation of the geometry-guided initiation rule using $LiBF_4$. (a) time-dependent photographs showing the gelation progress of the precursor solution; (b) ^1H NMR spectrum and (c) ^{13}C NMR spectrum of the resulting PDOL; (d) Nyquist plot of a SS/SS cell with $LiBF_4$-initiated PDOL.

To examine whether this structure–activity relationship extends to other planar Lewis acids, $LiBF_4$ (which generates the planar BF_3 intermediate) was also tested as an initiator. As shown in Fig. S5, the $LiBF_4$-initiated PDOL showed gelation within 6 h, a

monomer conversion of 93.1%, and a bulk impedance comparable to that of the $LiPO_2F_2$-initiated system, markedly superior to the $LiPF_6$-initiated counterpart.

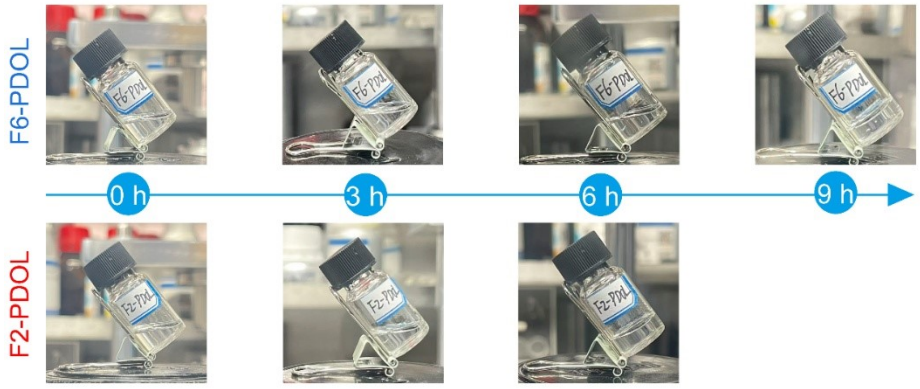

Fig. S6. Photographs showing the solidification progress of precursor solutions containing $LiPF_6$ or $LiPO_2F_2$ as initiators over time.

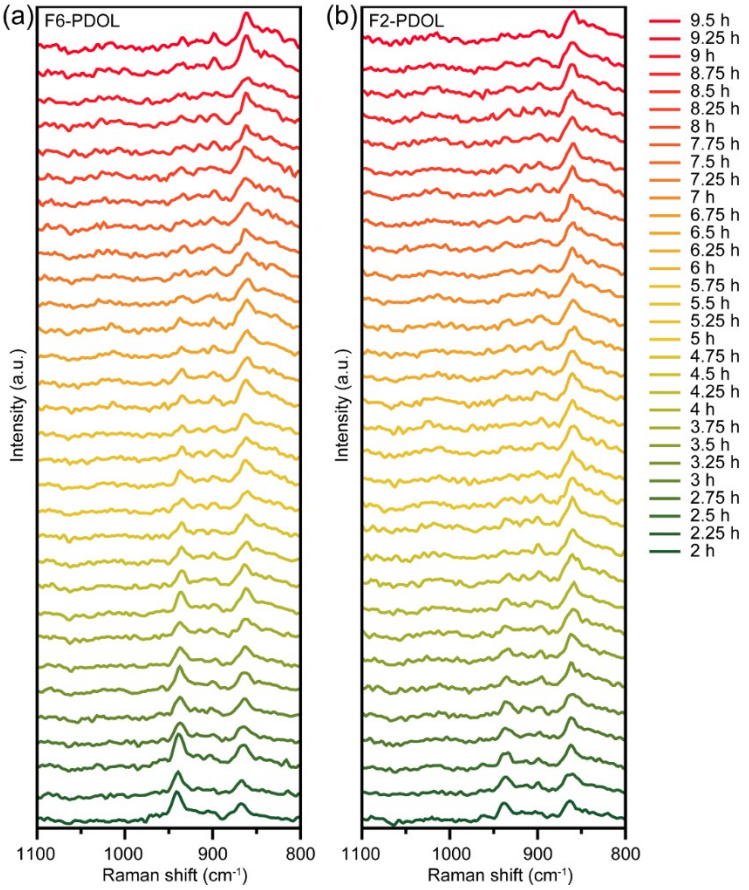

Fig. S7. Time-resolved in-situ Raman spectra of (a) F6-PDOL and (b) F2-PDOL electrolytes.

Table S2. GPC data of F6-PDOL and F2-PDOL before and after 80 ℃ treatment.

	M_n	M_w	Polydispersity
F6-PDOL	50514	52237	1.03
F2-PDOL	39746	45849	1.19
F6-PDOL (80 ℃ treated)	1227	1716	1.40
F2-PDOL (80 ℃ treated)	37002	41530	1.12

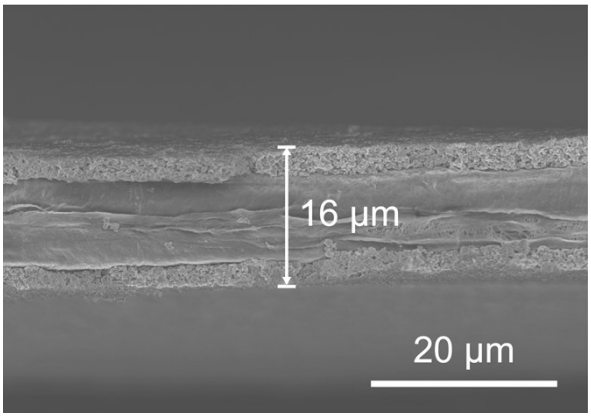

Fig. S8. Cross-sectional SEM image of the F2-PDOL electrolyte membrane.

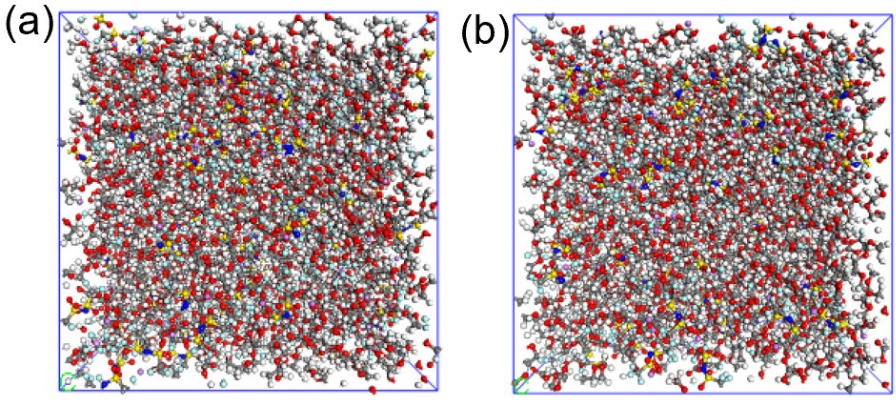

Fig. S9. Snapshots of the MD simulation boxes of (a) F6-PDOL and (b) F2-PDOL.

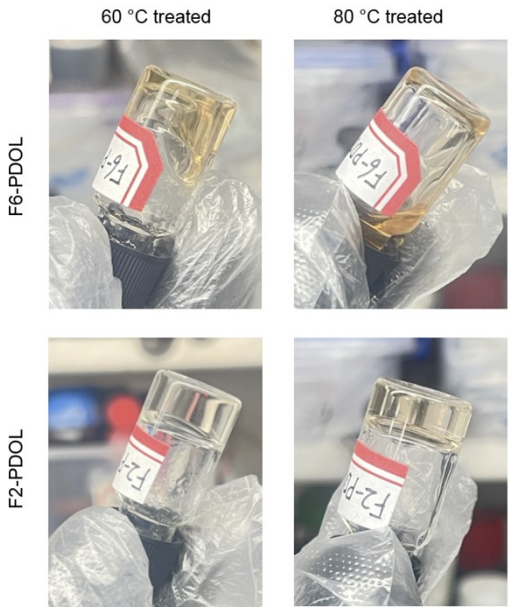

Fig. S10. Photographs of F6-PDOL and F2-PDOL after thermal aging at 60 °C and 80 °C, respectively.

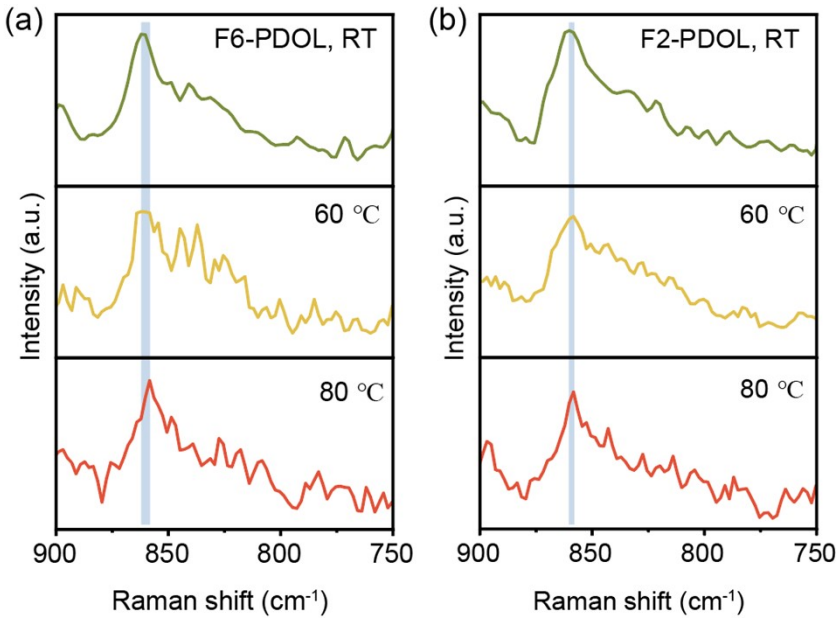

Fig. S11. Raman spectra of F6-PDOL and F2-PDOL at room temperature, 60 °C and 80 °C.

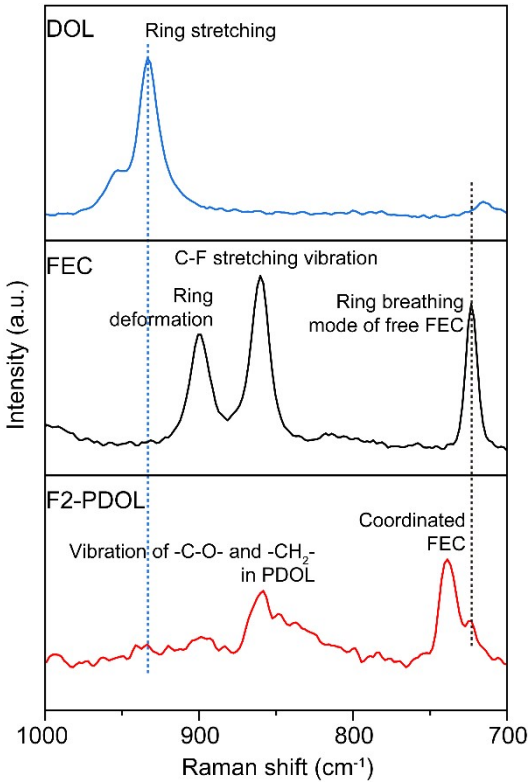

Fig. S12. Raman spectra of DOL and FEC solvents, and the F2-PDOL electrolyte.

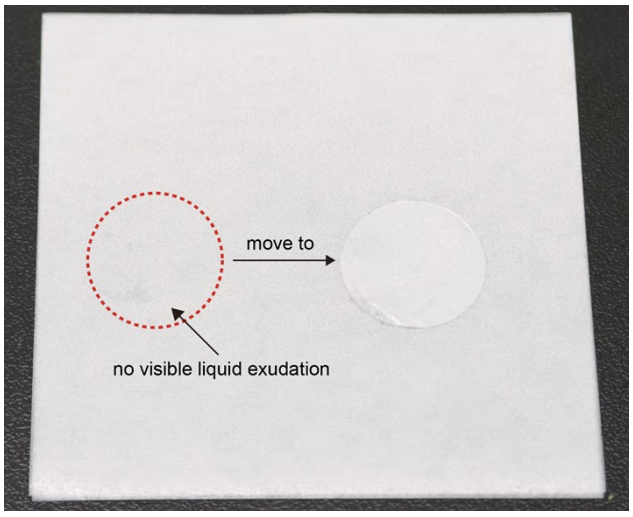

Fig. S13. Photograph of the F2-PDOL electrolyte membrane after heating at 80 °C for 30 min on weighing paper and then being moved aside, showing no visible liquid exudation at its original position.

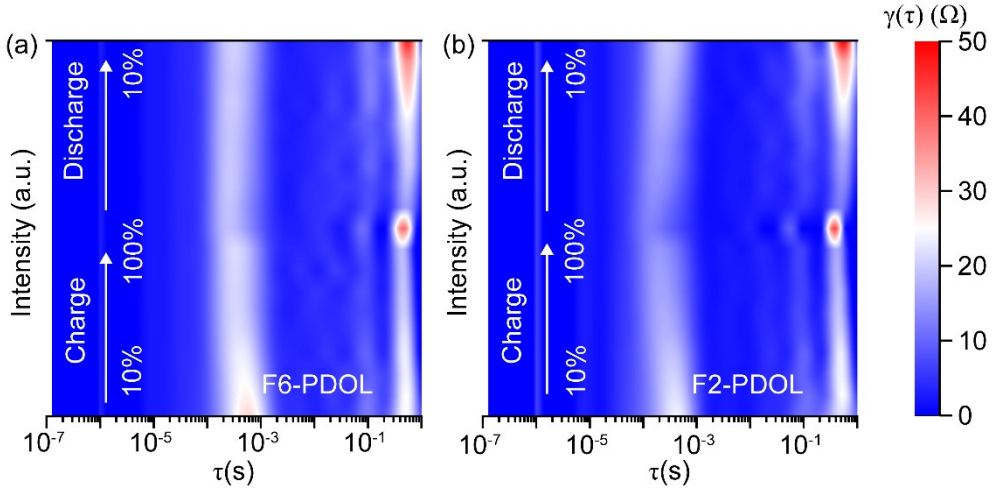

Fig. S14. In-situ EIS and corresponding distribution of relaxation times (DRT) analysis for LFP/Li cells with (a) F6-PDOL and (b) F2-PDOL.

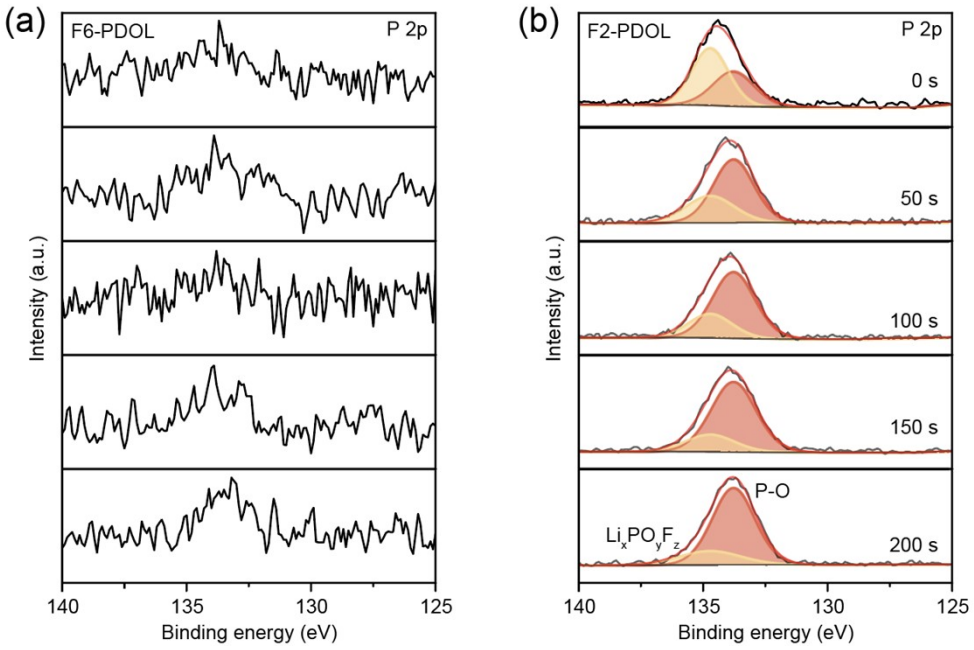

Fig. S15. P 2p XPS spectra of lithium anodes retrieved from LFP/Li cells after 100 cycles for (a) F6-PDOL and (b) F2-PDOL.

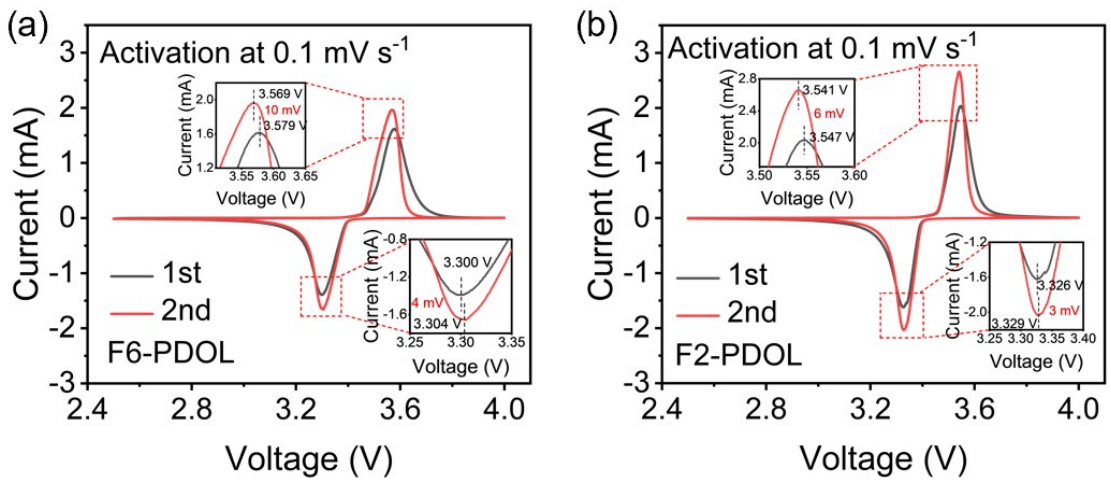

Fig. S16. CV curves of LFP/Li cells with (a) F6-PDOL and (b) F2-PDOL.

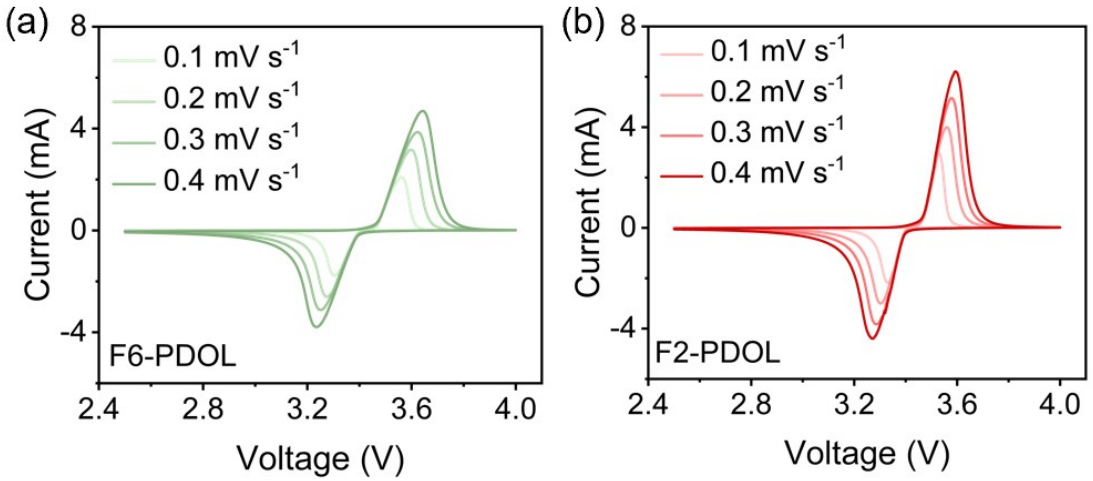

Fig. S17. CV curves measured at multiple scan rates for LFP/Li cells with (a) F6-PDOL and (b) F2-PDOL.

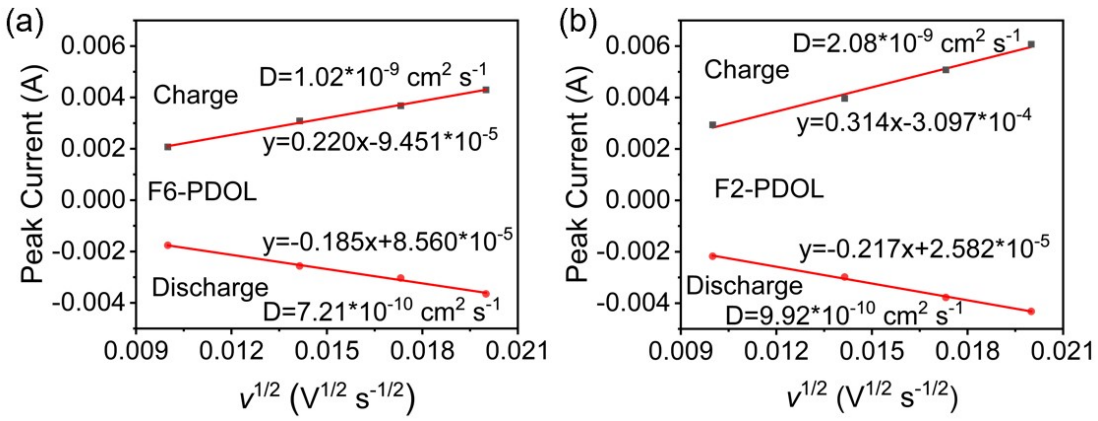

Fig. S18. Linear fitting of peak current versus scan rate from CV curves in Fig. S17. (a) F6-PDOL. (b) F2-PDOL.

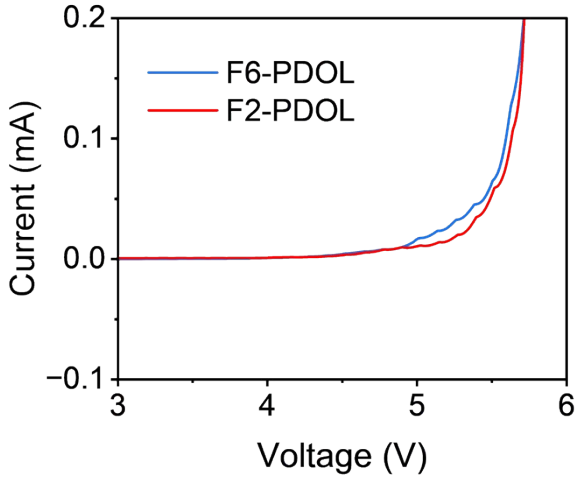

Fig. S19. LSV curves of (a) F6-PDOL and (b) F2-PDOL.

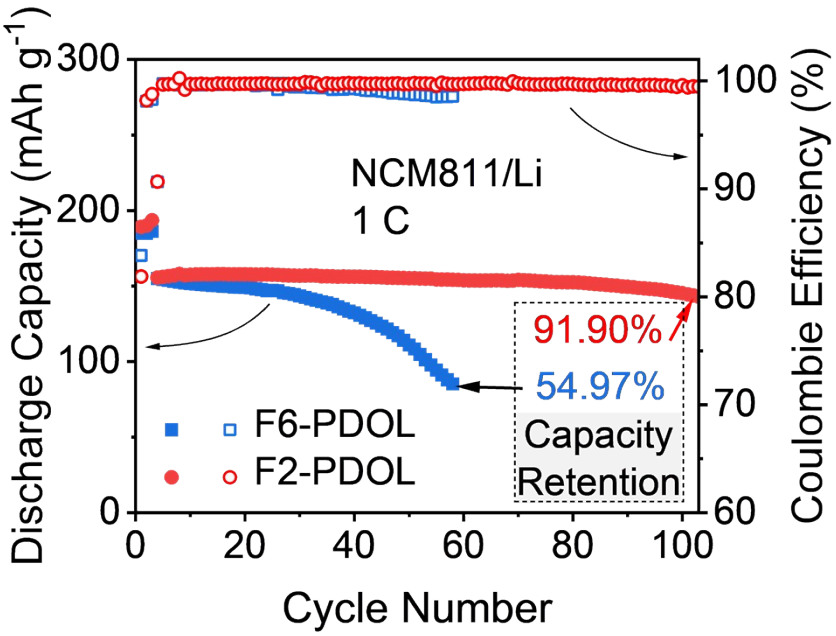

Fig. S20. Long-term cycling performance of NCM811/Li cells with (a) F6-PDOL and (b) F2-PDOL at 1 C. Cells were cycled between 2.8 and 4.3 V.

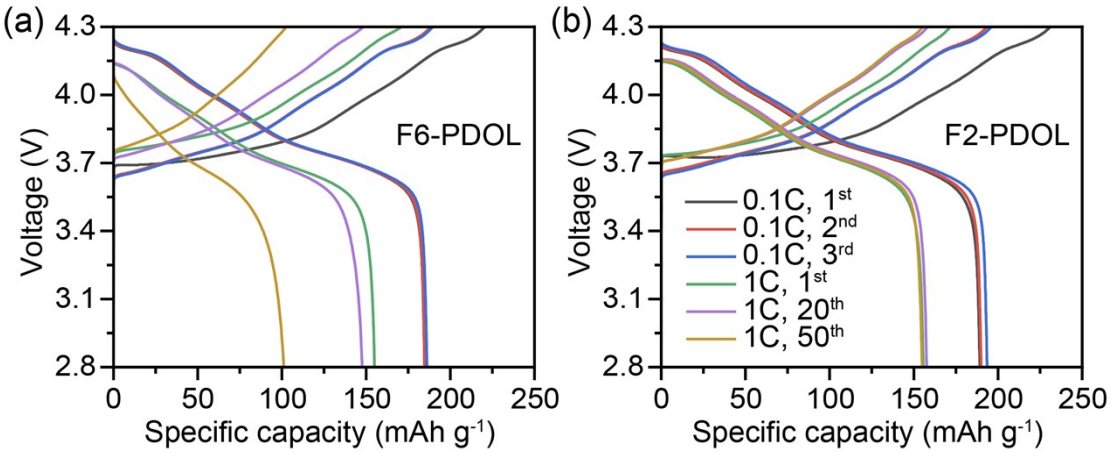

Fig. S21. Voltage profiles of NCM811/Li cells: (a) F6-PDOL and (b) F2-PDOL.

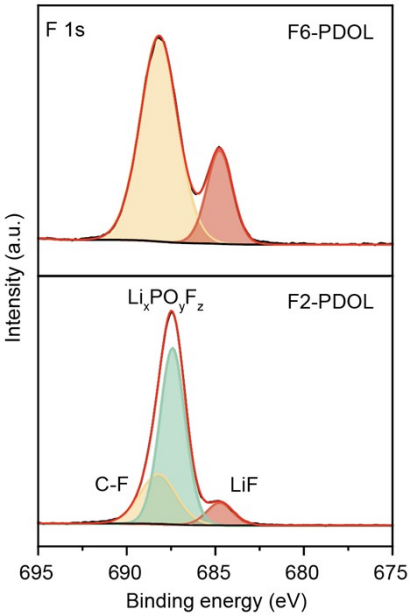

Fig. S22. F 1s XPS spectra of tested NCM811 cathodes after 50 cycles.

Table S3 Performance comparison with reported PDOL-based electrolytes in the literature.

Electrolyte	Polymerization degree	σ at RT[a] (mS cm^{-1})	ESW[b]	Cell performance	Ref.
Introducing IPTS[c] into LiDFOB-initiated PDOL	61%	0.28	4.9 V	LFP/Li, 1 C, 200 cycles, retention of 89.2%.	7
$In(OTf)_3$-initiated PDOL	95.7%	0.71	4.5 V	LFP/Li, 1 C, 300 cycles, retention of 85%.	8
$Ga(OTf)_3$-initiated PDOL	90.7%	0.5	4.1 V	LFP/Li, 1 C, 200 cycles, retention of 90.2%.	9
THB[d] -initiated PDOL	-	0.5074	4.2 V	LFP/Li, 1 C, 300 cycles, retention of 98.64%.	10
$AlCl_3$-initiated PDOL	87%	5	4.4 V	LFP/Li, 0.5 C, 280 cycles, retention of 92.7%.	11
Introducing KBTO[e] into $LiPF_6$-initiated PDOL	-	0.22	4.9 V	LFP/Li, 0.5 C, 250 cycles, retention of 93.1%; NCM811/Li, 1 C, 150 cycles, retention of 79.9%.	12
LiDFOB-initiated PDOL	-	0.36	4.8 V	LFP/Li, 60 ℃, 0.5 C, 150 cycles, retention of 82%.	13
Introducing $LiNO_3$/DMSO[f] into LiDFOB-initiated PDOL	88.8%	1.65	>4.3 V	LFP/Li, 1 C, 500 cycles, retention of 73.1%.	14
Mg^{2+}-containing MMT[g]-	92.2%	0.212	5.3 V	NCM811/Li, 0.5 C, 100	15

initiated PDOL				cycles, retention of 87.3%	
LiDFOB-initiated PDOL	-	0.45	5 V	LFP/Li, 0.4 C, 250 cycles, retention of 76.85%.	[16]
PFDA[h]-initiated PDOL	88.7%	1.6	4.8 V	LFP/Li, 0.5 C, 300 cycles, retention of 85%.	[17]
SnF_2-initiated PDOL	-	0.017	-	LFP/Li, 45 ℃, 0.15 C, 350 cycles.	[18]
Introducing TBB[i] into TFB[j]-initiated PDOL	87.8%	0.113	4.5 V	NCM811/Li, 0.5 C, 100 cycles, retention of 83.2%.	[19]
Introducing $N_{1222}FSI$[k] into LiDFOB-initiated PDOL	90.5%	0.981	5.8 V	NCM622/Li, 0.2 C, 100 cycles, retention of 81.3%.	[20]
Introducing SL[l] and SbF_3 into LiDFOB-initiated PDOL	-	0.322	5.14 V	LFP/Li, 0.5 C, 300 cycles, retention of 74.4%.	[21]
$InCl_3$-initiated PDOL	96.2%	2.47	4.1 V	LFP/Li, 0.5 C, 200 cycles, retention of 91.9%.	[22]
InF_3-initiated PDOL	94%	0.089	4.7 V	LFP/Li, 1 C, 300 cycles, retention of 90%.	[23]
$SnCl_4$-initiated PDOL	90.5%	2	4.7 V	LFP/Li, 0.2 C, 100 cycles, retention of 70%.	[24]
Introducing TMSO[m] into TFB-initiated PDOL	-	0.0836	5.1 V	LFP/Li, 0.5 C, 160 cycles, retention of 97%; NCM811/Li, 0.3 C, 100 cycles, retention of 90%.	[25]
PDOL with ternary salts ($LiPF_6$, LiTFSI, LiFSI)	-	0.618	4.5 V	LFP/Li, 0.5 C, 500 cycles, retention of 79.1%.	[26]
$LiPO_2F_2$-initiated PDOL	87.61%	0.19	~4.5 V	LFP/Li, 1 C, 400 cycles, retention of 96.21%; LFP/Li, 60 ℃, 1 C, 100 cycles, retention of 92.41%; NCM811/Li, 1 C, 100 cycles, retention of 91.90%.	This work

[a]RT: room temperature.

[b]ESW: electrochemical stability window.

[c]IPTS: trimethylsilyl isocyanate.

[d]THB: tris(hexafluoroisopropyl) borate.

[e]KBTO: epoxy-functionalized $BaTiO_3$.

[f]DMSO: dimethyl sulfoxide.

[g]MMT: montmorillonite.

[h]PFDA: perfluorodecanoic acid.

[i]TBB: tributyl borate.

[j]TFB: tris(pentafluorophenyl)borane.

[k]$N_{1222}FSI$: triethylmethylammonium bis(fluorosulfonyl)imide.

[l]SL: sulfolane.

[m]TMSO: 1,3-bis(3-glycidoxypropyl) tetramethyl disiloxane.

References

1 T. H. Wan, M. Saccoccio, C. Chen and F. Ciucci, *Electrochim. Acta*, 2015, **184**, 483–499.

2 Y. Lu, C.-Z. Zhao, J.-Q. Huang and Q. Zhang, *Joule*, 2022, **6**, 1172–1198.

3 A. D. Becke, *J. Chem. Phys.*, 1993, **98**, 5648–5652.

4 P. J. Stephens, F. J. Devlin, C. F. Chabalowski and M. J. Frisch, *J. Phys. Chem.*, 1994, **98**, 11623–11627.

5 R. L. C. Akkermans, N. A. Spenley and S. H. Robertson, *Mol. Simul.*, 2021, **47**, 540–551.

6 D. Chen, T. Zhu, M. Zhu, P. Kang, S. Yuan, Y. Li, J. Lan, X. Yang and G. Sui, *Small Methods*, 2022, **6**, 2201114.

7 J. Cao, M. Zhang, J. Xu, M. Wang, B. Hong and Y. Lai, *ChemSusChem*, 2025, **18**, e202402028.

8 H. Deng, X. Yang, H. Chen, D. Ye, X. Jiang, Y. Chen and C. Wang, *J. Energy Storage*, 2024, **100**, 113693.

9 B. Lu, L. Hu, W. Zhang, J. Zhang, Y. Xia, Y. Gan, X. He, X. Xia, R. Fang and H. Huang, *ACS Appl. Mater. Interfaces*, 2024, **16**, 55314–55324.

10 T. Li, K. Chen, B. Yang, K. Li, B. Li, M. He, L. Yang, A. Hu and J. Long, *Chem. Sci.*, 2024, **15**, 12108–12117.

11 J. Yu, S. Hong, M. Park, M. Kwak, S. Kim, J. Heo and W. B. Kim, *Adv. Sci.*, 2026, **13**, e19181.

12 J. Xu, A. Wang, Z. Qiu, J. Fang, Q. Lu, S. Song, Z. Lin, S. Tian, M. Sun, J. Lv, W. Yu, S. Yang, X. Qi, W. Guo, J. Li, F. Shen and X. Han, *J. Colloid Interface Sci.*, 2026, **704**, 139442.

13 P. Li, X. Liu, Y. Luo and Z. Rao, *J. Colloid Interface Sci.*, 2025, **700**, 138329.

14 Y. An, R. Li, C. Fang, W. Hu, Y. Yang, A. Li, D. Huang, H. Chu, S. Gao, Y. Wang,

J. Zheng, Y. Liu and R. Zou, *Chem. Eng. J.*, 2025, **513**, 162822.

15 H. Xu, J. Mi, J. Ma, Z. Han, S. Lv, L. Chen, J. Zhang, K. Yang, B. Li, Y. Li, X. An, Y. Ma, S. Guo, H. Su, P. Shi, M. Liu, F. Kang and Y. He, *Energy Environ. Sci.*, 2025, **18**, 4231–4240.

16 C. Lei, T. Zhou, M. Zhang, T. Liu, C. Xu, R. Wang, X. He and X. Liang, *Adv. Sci.*, 2024, **11**, 2405482.

17 X. Li, Q. Liu, Y. Wang, J. Lin, C. Ji, Y. Yuan, B. Zhao and X. Xiong, *Small*, 2025, **21**, 2411104.

18 W. Li, J. Gao, H. Tian, X. Li, S. He, J. Li, W. Wang, L. Li, H. Li, J. Qiu and W. Zhou, *Angew. Chem. Int. Ed.*, 2022, **61**, e202114805.

19 K. Xi, Y. Wang, C. Li, Y. Lei, X. Xu, L. Wei and Y. Gao, *J. Colloid Interface Sci.*, 2025, **679**, 1277–1287.

20 A. Hu, Z. Liao, J. Huang, Y. Zhang, Q. Yang, Z. Zhang, L. Yang and S.-i. Hirano, *Chem. Eng. J.*, 2022, **448**, 137661.

21 B.-H. Zhang, W.-X. Wen, H.-Y. Wang, Y.-L. Hou, J.-Z. Chen and D.-L. Zhao, *Chem. Eng. J.*, 2023, **472**, 144990.

22 T. Yang, W. Zhang, Y. Liu, J. Zheng, Y. Xia, X. Tao, Y. Wang, X. Xia, H. Huang, Y. Gan, X. He and J. Zhang, *Small*, 2023, **19**, 2303210.

23 X. Yang, D. Ye, C. Wang, Y. Chen, X. Jiang, Y. Yang and Z. Liu, *J. Power Sources*, 2024, **600**, 234262.

24 Q. Hao, Y. Gao, F. Chen, X. Chen, Y. Qi and N. Li, *Chem. Eng. J.*, 2024, **481**, 148666.

25 J. Cui, Y. Du, L. Zhao, X. Li, Z. Sun, D. Li and H. Li, *Chem. Eng. J.*, 2023, **461**, 141973.

26 Z. K. Liu, J. Guan, H. X. Yang, P. X. Sun, N. W. Li and L. Yu, *Chem. Commun.*, 2022, **58**, 10973–10976.